Contents

List of Figures

List of Tables

4

1. Introduction

Pipeline transport of solid-liquid sludge is an essential operation in many areas, such as mining and chemical processing. This comes down to the fact that pipelines are more efficient and environmentally friendly than railway transportation. Yet, the transported fluid may be highly viscous and have complex rheology. Moreover, the flow within the pipe is generally highly turbulent and complex (Lahiri and Ghanta [1]) and problems like pipe plugging, and solid sedimentation could occur. Therefore, to ensure a continuous and optimal flow, different parameters should be controlled. In particular, the distribution of solids and the pressure drop within the pipeline represent a serious concerns to engineers, since their determination involves considerable technical difficulties. Thus, having means to predict the physics of the slurry flow is essential for the control of the pipeline process. The rapid increase in computational power has made it possible to widely distribute different tools and techniques, capable of modeling complex flows in real-dimensional geometries. This paved for a better handling of such flows by complementing empirical methods with digital simulations. Therefore, Computational Fluid Dynamics (CFD) has appeared as an effective tool to model and predict unknown or particular slurry flow scenarios (Xia and Sun [2]), and it can provide a series of monitoring information, which is difficult to achieve by experience alone. The advantages of CFD can be categorised as (Wanot [3]):

- It provides a detailed understanding of flow distribution, mass and heat transfer, particulate separation, etc. Consequently, all these will lead to a much better and deeper understanding of what is happening in a particular process or system.

- It is able to reduce scale-up problems because the models are based on fundamental physics and are scale independent.

- It is particularly useful in simulating conditions where it is not possible to take detailed measurements.

5

1.1. CFD approaches for multiphase flows

Generally, the CFD approaches for the simulation of slurry flows can be classified into: Eulerian-Lagrangian approaches ([4]), where the liquid phase is modeled as a continuum and solved in an Eulerian cell-based framework, whereas the behavior of the solid phase is obtained by the Discrete Particle Method (DPM), in which the individual trajectories of computational particles are calculated in a Lagrangian fashion. Secondly, there is the Eulerian-Eulerian approaches ([4]), where both phases are modeled as interpenetrating continua, and two sets of conservations equations are solved jointly in the Eulerian framework. The coupling between the two phases depends on the amount of solids in the flow, and it ranges from one-way coupling for dilute slurries (i.e. the particles do not affect the liquid flow field) to four-way coupling for dense slurries (where the particle-particle and particle-fluid interactions are important as well). This approach characterizes the majority of the earlier CFD investigations of slurry pipe flows which provides a good compromise between accuracy and computational cost. Yet three models are possible within this approach. Table 1 shows a comparison of the latter models.

Table 1: Comparison between Euler-Euler models

VOF	Mixture Model	Multi-phase Eulerian Model
Modelling non-miscible fluid	Model used if there is a wide distribution of dispersed phases	Interphase laws available.
A single set of motion equations.	Interphase laws not available.	More precise.
Examples: Examples: free surface flow ([?])), large bubbles in a liquid ([?])), stratified flow ([?])).	Examples: particle-laden flow* with low load ([?]), bubble flow, sludge flow ([14]).	Examples: sludge flow ([?]), sedimentation ((([?]), fluidized beds ([?])).

*Particle-laden flow = Particle charge flows refer to a two-phase flow in which one of the phases is continuously connected and the other phase consists of small immiscible particles and typically diluted.

6

1.2. Problem Description

This work concerns the transport of phosphate ores in the context of an industry 4.0. The process begins with the extraction of ore that is transported as pulp (Water + Phosphate) in a pipe (pipeline), from the mine to the industrial units for processing (Figure 1). This pulp is characterized by a solid volume concentration that goes up to 40 %, it contains rigid solid particles of random shapes having an equivalent spherical diameter ranging from $44\mu_m$ to $400\mu_m$. The ore particles are characterized by an average total porosity of 20 % by volume, then an effective density of $2600kg/m3$ when the pores are filled with water. The operation of the phosphate slurry pipe is controlled by a series of pressure and choke stations. The pipeline receives the phosphate ore, of different qualities, from four different washing stations, which gives it variable flow properties (viscosity, density, speed, pressure...). The phosphate pulp is transported in batches, separated by batches of water to control the quality and flow of the pulp (Figure 2). The main challenge of the work to be carried out in the context of this thesis is is to set the basis for an intelligent control for the transport process, based on computational fluid dynamics (CFD) simulation models. This system will ensure optimal operation of the process, predict the evolution of certain critical parameters and contribute to operational decision-making. From an application point of view, among the industrial stakes of the project of this thesis:

- Increase productivity (volume sent by the pipe);

- Secure the pipe by mastering the characteristics of the pulp;

- Predict solid concentration profiles and pressure losses in the pipeline;

- Optimize pipe operation according to pulp quality;

- Optimize energy consumption, etc;

2. Literature Review : slurry pipes modeling and simulation

2.1. CFD studies

A summary of the most relevant numerical studies on slurry flows in horizontal pipes published so far are reported, alongside with the adopted modelling approach. Beginning with Eulerian-
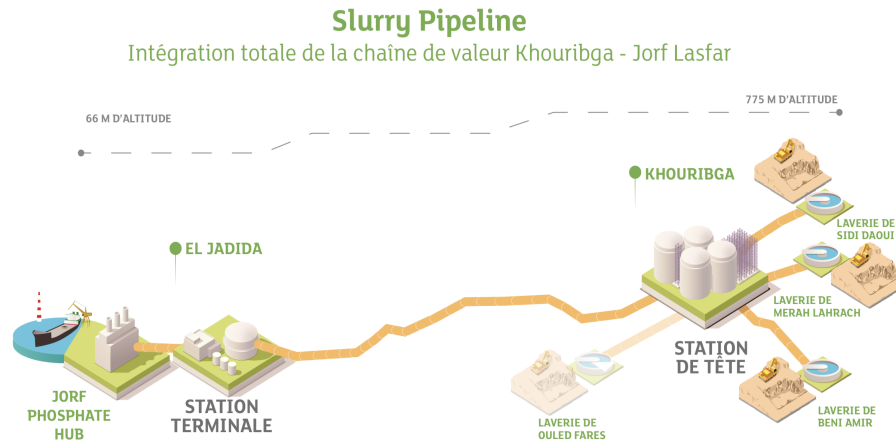
Figure 1: Transport process of phosphate slurry
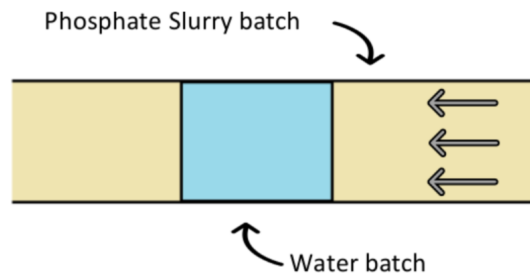
Figure 2: Phosphate slurry flow

Lagrangian approach, this latter was employed for this kind of applications for sand-water slurry by Capecelatro and Desjardins [5], where the Large Eddy Simulation (LES) method Versteeg and Malalasekera [6] has been used to simulate the turbulent flow of the liquid phase, while the solid phase was treated by DPM. Arolla and Desjardins [7] used the same numerical setup to characterize a sand-water flow pattern for increasing values of liquid superficial velocity. Always in the Eulerian-Lagrangian approach but this time it was employed with different characteristics such as transportation of coarse NaCl particles in brine by Uzi and Levy [8], where the liquid phase is handled by a computationally cheaper Reynolds-Average Navier-Stokes (RANS) technique, to examine the effects of the operating conditions on the flow. Concerning the mixture model, and at the start of 21st century, Ling et al. [9] performed CFD simulations for sand-water slurry flows

through horizontal pipes, where a simplified 3D algebraic slip mixture (ASM) model is introduced along with RNG k–ϵ turbulent model to obtain the precise numerical solution in fully developed turbulent flow. They compared CFD results of mean pressure gradients with experimental results, and found a big discrepancy between them takes place when the mean velocities of slurry flows are lower than corresponding critical deposition velocities. Lin and Ebadian [10] numerically investigated sand–water slurry flows in the entrance region of horizontal pipe, again using ASM model, and have focused mainly on illustrating and comparing the developing processes of various flow parameters. Silva et al. [11] performed simulations for Saline Water-Glass beads slurry using Mixture Model coupled with a High Reynolds k–ϵ turbulence model, results were validated with data attained with an Electrical tomography apparatus. The model produced accurate representations for the highest flow rates, while showing some deviations for the lower flow rate. However, the majority of the earlier CFD investigations of slurry pipe flows were performed using the Two Fluid Model. In most TFMs, constitutive equations for the solid phase derived from the Kinetic Theory of Granular Flow (KTGF) were employed. The most relevant numerical studies on slurry flows in horizontal pipes published so far, the study of Hernandez et al. [12] for sand-water slurry, where homogeneous and heterogeneous flow regimes without bed were considered along with predictions of pressure gradients at the fully developed zone, a year after Ekambara et al. [13] investigated the effect of in situ solids volume concentration, particle size, mixture velocity, and pipe diameter, on local time-averaged solids concentration profiles, particle and liquid velocity profiles, and frictional pressure loss. Excellent agreement between the predicted and the experimental was obtained. Chen et al. [14] used the same numerical configuration to simulate flow of coal-water slurries (CWS) in a horizontal pipeline, with bimodal distribution for coal particles. They found out that the simulation results of the binary solid phase model is closer to experimental data, as compared to the results of the single solid phase model. Bossio et al. [15] focused on modeling of non-newtonien Laterite-Sand slurry where the mean pressure gradients were compared with experimental data. Antaya et al. [16] performed simulations for concentrated mixtures of sand-water slurry with monosized and bimodal particle sizes. Shear stress model (SST) was tested in addition to the k–ϵ model to treat the turbulence of the continuous phase. Success has been achieved in the use of k–ϵ model, with the SST model being superior, especially in the near-wall region.

However Kaushal et al. [17], tried both Mixture and two-phase model to simulate mono-dispersed fine particles at high concentration of glass beads mixed with water. They proved again the failure of the Mixture Model predictions at high velocities and high solid concentrations compared to TFM. [18] worked on an unusual type of slurry flows which is Slush nitrogen flow using the 2D Eulerian – Eulerian multiphase approach. The per-phase k–ϵ turbulence model is used in the study to model the turbulent two-phase flow. The effects of the flow velocity and the mean solid volume fraction on the flow characteristics of slush nitrogen are investigated numerically in this study. The same team in very next year Jiang and Zhang [19] investigated the same slush and nitrogen flow. Based on the experimental and numerical results they distinguished three flow patterns which for each one they had studied the variation of pressure drop. And they obtained the general correlation of the friction factor with the slush Reynolds number of slush nitrogen with various solid volume fractions. Wang et al. [20] applied the two fluid model to describe an ice slurry flow without considering ice melting. After validation of the model with experimental data, it was used to investigate the distributions of ice slurry flow, ice particle concentration and pressure drop in horizontal, vertical and 90 elbow pipes respectively. They found that for pressure drop, The numerical model is found being able to provide results in good agreement with the experimental data where the relative errors are limited to 20%. Messa et al. [21] developed a new two-fluid model for the simulation of Sand and Glass beads Water slurry. Contrary to previous works with TFM models, they did not integrate the kinetic theory of granular flows to determine solid viscosity. They studied the effect of the wall boundary condition for the solid phase on the pressure gradient, where they found that the best match between measurements and computations is obtained when the equilibrium logarithmic law of Launder and Spalding for smooth walls is applied to the solid phase. Then Messa et al. [22] used the new TFM model to simulate a fully-suspended Sand-Water slurry flow in horizontal pipes and bends. They claimed that the model is robust and numerically stable, and requires relatively short computer time to provide a converged steady-state solution. The novelty of the proposed model and its better performance compared to similar ones reside in the method of accounting for some key physical mechanisms governing these flows, namely turbulent dispersion, interphase friction, and viscous and mechanical contributions to friction. Messa and Malavasi [23] further modified Messa et al. [22] model by incorporating a new wall boundary

condition for the solid phase, a more general correlation for the viscosity of the slurry, accounting for particle shape along with a different solution algorithm. These changes resulted in low computational effort with improved performance. They verified the modified model by comparing its outcomes with experimental results for sand-water slurries available in the literature. returning to the TFM combined with KTGF, Gopaliya and Kaushal [24] studied the effects of grain size on various Sand-Water slurry flow parameters. They found that at the same volumetric concentration, pressure drop increases with increase in grain size. Hashemi et al. [25] performed experiments in a 265 mm diameter pipe loop with sand-in-water slurries, then selected experimental conditions were numerically simulated using a commercial CFD package, ANSYS CFX. They noticed that the agreement between the numerical results and the experimental data is concentration dependent, with relatively closer agreement at lower concentrations. Kumar et al. [26] presented experimental data of iron-ore slurry flow cases through 105 mm pipe, the obtained results are validated using TFM-KTGF model. Results reflect good resemblance between measured and predicted pressure drops, solid concentrations and velocity profiles. Singh et al. [27] investigated the flow characteristics of coal water slurry having high solid concentrations in slurry pipeline. They have noticed that the coal-water slurry shows Newtonian behaviour at 30% solid concentration (by-weight) and beyond this it depicts non Newtonian pseudo plastic behavior. In this study also SST k-ω turbulence model was found a better predictor over other models namely Standard k-ϵ, RNG k-ϵ, Realizable k-ϵ and Standard k-ω models. A year after Li et al. [28] developed a useful three-dimensional multiphase hydrodynamic model based on the kinetic theory of granular flow, for simulating multi-sized glass beads-water slurry transport through pipelines, to investigate the distributions of solid concentration, flow velocity, granular pressure, and wall shear stress. The simulation result of different-sized particle behaviors in multi-sized slurry has significant reference value. Li et al. [29] also in the same year studied the effect of interaction of particles with different sizes on particle kinetics in multi-sized slurry, first They concluded that the speed of resistance increase in a graded slurry is more gradual than in a single-sized slurry with the same conditions as the solid concentration increases,then they found that the wall shear stress of coarse particles is significantly reduced by the existence of fine particles with increasing flow rate and solid concentration, and finally they affirmed that the existence of fine particles significantly re-

11

duces the collision intensity of coarse particles and velocity fluctuations in the multi-sized slurry. Recently, Messa and Matoušek [30] considered again the same Two Fluid Model, but this time for a deeper physical interpretation, and to provide recommendations of general validity. For the sake of generality and strength of the numerical model, three different data sets were considered for the experimental verification of the model, resulting in 108 different simulation scenarios covering a wide range of pipe diameters, solid concentrations, and slurry velocities.

2.1.1. Summary on models classification

Following the literature review presented above, our CFD approach will be based on the Eulerian model (Two Fluid Model) as it is the most complete model and the most used one to deal with suspensions transport issues, and is confirmed to be the most accurate and gives generally good results. While mixture model fails to predict pressure drops correctly and the amount of error increases rapidly with the slurry concentration (Kaushal et al. [17]). The main conclusions from the literature review are summed in table 2. The description of the TFM model is given in section 3.1. The dynamics of the solid phase is modeled by the KTGF to consider both particle collisions and frictions. Also, based on the previously cited works, the turbulence of the continuous phase is treated by the k-ϵ based models, that generally shows reasonable robustness, and give reasonable accuracy for a wide range of applications. Yet, even though success is usually achieved using models based on the k-epsilon, it should be made clear that they may not perform well in the region near the wall (Antaya et al. [16]). Therefore, a near-wall treatment model is presented in section 3.4, to address the weak performance of the choosed turbulence models in this area of the pipe.

Table 2: Summary on models classification

Models	Conclusions
DPM (Eulerian-Lagrangian Approach)	The discrete phase must be present at a fairly low volume fraction, usually less than 10-12%
Mixture Model	There is a big discrepancy between CFD results with experimental, especially at lower flow rates.
TFM Model	TFM is accurate and gives generally good results comparing to the mixture model. TFM results are better and closer to the experimental data in the case of bimodal particle sizes or at higher velocities.

In fact, modern modeling strategies, for industrial processes, integrates usually 3D simulation techniques using computational fluid dynamics (CFD) and/or discrete element methods (DEM). These 3D models are then integrated as surrogate models that can be used in operations simulation and monitoring tools (Decision Support Systems). Classically, response surface methodologies (RSM) are applied to build a polynomial surrogate model (Rabhi et al. [31]), but also in recent works machine leaning techniques such as artificial neural networks (ANN) can be used (Seong et al. [32]). The current modeling approach consists of constructing 3D models for different type of pipe elements (horizontal, inclined, bended pipes), and then use them to construct surrogates that models the pressure drop within each element. Such models can then be used in dynamical models for monitoring slurry pipe systems and to conduct sizing studies to cover variations in the operation conditions like inlet pressure and inlet flow rate. This approach will first be applied to a single fluid flow to validate the approach of constructing a surrogate pressure drop model through 3D numerical simulation, and then to slurry flows with solid volume fraction up to 25%.

A parametric analysis is conducted to investigate the impact of the variation in the particle size, solids concentration, and inlet velocity, on the solid concentration profile, the solid velocity profile and finally their effect on the variation in the pressure drop along the pipe. This analysis allows us to validates our simulations for turbulent slurry flows versus experimental data. The data used in this work is regarding a horizontal pipe case for Water-Sand slurry flow: transported solid volume

13

fraction between 19 % and 45 %; velocities between 1 m/s and 8.0 m/s; and particles sizes of 90

μ_m and 270 μ_m.

3. Theoretical and empirical models

3.1. Mathematical models

In the two-fluid Eulerian-Eulerian approach, each phase is described by a set of averaged conservation equations. The present formulation follows [33, 34]. A general discussion of how such models are derived via averaging can be found in [35]. Introducing the particle volume fraction field ϕ, the governing equations for the two phases are expressed as follows

$$
\begin{cases}
\partial_t \left(\varrho_{\mathfrak{f}} \phi_{\mathfrak{f}} \right) + \partial_i \left(\varrho_{\mathfrak{f}} \mathfrak{u}_{\mathfrak{p},i} \phi_{\mathfrak{f}} \right) = 0, \\
\varrho_{\mathfrak{f}} \phi_{\mathfrak{f}} \left(\partial_t \mathfrak{u}_{\mathfrak{f},i} + \mathfrak{u}_{\mathfrak{f},j} \partial_j \mathfrak{u}_{\mathfrak{f},i} \right) = \varrho_{\mathfrak{f}} \phi_{\mathfrak{f}} g_i - \phi_{\mathfrak{f}} \partial_i \mathfrak{p} + \partial_j \tau_{\mathfrak{f},ij} + \mathrm{F}_{\mathfrak{f},i},
\end{cases}
\tag{1}
$$

where the letter t represents the time and the symbols ∂_t and ∂_i denote the partial differential operators ∂/∂_t and $\partial/\partial x_i$, respectively. Furthermore, the summation convention for repeated indices is used. Here, $\phi_{\mathfrak{f}}$ is the volume fraction and $\varrho_{\mathfrak{f}}$ the density of the respective fluid. The velocity vector is denoted by $\mathfrak{u}_{\mathfrak{f}}$, the pressure by $\mathfrak{p}$, and the gravity by g. The index $\mathfrak{f}$ is symbolic for the solid and the fluid phase, e.g. the solid phase fraction may be denoted by $\phi_{\mathfrak{p}}$, the one of the continuous phase as $\phi_{\mathfrak{w}}$. The sum of the volume fraction of the different phases is always unity. The stress tensor is evaluated as $\tau_{\mathfrak{f},ij} = 2\phi_{\mathfrak{f}}\mu_{\mathfrak{f}} \left(S_{\mathfrak{f},ij} - S_{\mathfrak{f},kk}\delta_{ij}/3 \right)$ with $S_{ij} = \left(\partial_j \mathfrak{u}_{\mathfrak{f},i} + \partial_i \mathfrak{u}_{\mathfrak{f},j} \right)/2$. The last term $\mathbf{F}_{\mathfrak{f}}$ in (1) denotes the momentum transfer between the phases. It is decomposed into drag forces $\mathbf{F}_{\mathfrak{f}}^{\mathrm{d}}$, lift forces $\mathbf{F}_{\mathfrak{f}}^{\mathrm{l}}$, and turbulent dispersion forces $\mathbf{F}_{\mathfrak{f}}^{\mathrm{vm}}$ and it is expressed therefore as

$$
\mathbf{F}_{\mathfrak{f},i} = \mathbf{F}_{\mathfrak{f}}^{\mathrm{d}} + \mathbf{F}_{\mathfrak{f}}^{\mathrm{l}} + \mathbf{F}_{\mathfrak{f}}^{\mathrm{vm}}.
\tag{2}
$$

In the present two-fluid calculation, the following functional forms [36] are retained

$$
\begin{cases}
\mathbf{F}_{\mathfrak{f}}^{\mathrm{d}} = \frac{3}{4}\frac{\varrho_{\mathfrak{w}}}{\mathrm{d}_{\mathfrak{s}}} C_{\mathrm{d}} \|\mathfrak{u}_{\mathfrak{w}} - \mathfrak{u}_{\mathfrak{s}}\| \left(\mathfrak{u}_{\mathfrak{w}} - \mathfrak{u}_{\mathfrak{s}} \right), \\
\mathbf{F}_{\mathfrak{f}}^{\mathrm{l}} = \varrho_{\mathfrak{w}} C_{\mathrm{l}} (\mathfrak{u}_{\mathfrak{w}} - \mathfrak{u}_{\mathfrak{s}}) \times \left(\nabla \times \mathfrak{u}_{\mathfrak{w}} \right), \\
\mathbf{F}_{\mathfrak{f}}^{\mathrm{vm}} = \varrho_{\mathfrak{w}} C_{\mathrm{vm}} \left(\mathrm{D}_t^{\mathfrak{w}} \mathfrak{u}_{\mathfrak{w}} - \mathrm{D}_t^{\mathfrak{s}} \mathfrak{u}_{\mathfrak{s}} \right),
\end{cases}
\tag{3}
$$

14

where $D_t^{\dagger} = \partial_t + u_{f,j}\partial_i$ stands for the substantive derivative corresponding to each phase $\dagger$, and C_d, C_l and C_{vm} are the drag, lift and virtual mass coefficients, respectively. For the drag coefficient, the solid particle drag model of Wen and Yu [37] is retained, which reads

$$
C_d = \begin{cases} \frac{24}{\mathcal{R}e}\left(1 + 0.15\mathcal{R}e^{0.687}\right)(1 - \phi_s)^{-2.7} & \text{, if } \mathcal{R}e \leq 10^3, \\ 0.44\,(1 - \phi_s)^{-2.7} & \text{, if } \mathcal{R}e \geq 10^3, \end{cases} \tag{4}
$$

where $\mathcal{R}e = \varrho_s\|u_r\|d_s/\mu_s$ is the Reynolds number bases on the particle diameter d_s and the relative velocity $u_r = u_w - u_s$. For virtual mass coefficient C_d, a fixed value of 0.5 is used throughout the present study [38].

The solid phase is modelled in this Eulerian framework as an interpenetrating fluid but with a viscosity that is determined by the kinetic theory of granular flows

3.1.1. Solid-phase viscosity

Solid-phase viscosity is determined using Kinetic Theory of Granular flows(KTFG) which is based on the kinetic theory of gases in a generalized way to take into account collisions of inelastic particles to define a granular temperature θ in solid phase which directly affects the phase stress tensor ([39]). Analogical to the thermodynamic temperature for gases, the granular temperature $\Theta = \frac{1}{3} < v_s'^2 >$ was introduced as a measure for the energy of the fluctuating velocity of the particles Lun et al.1987. The equation of conservation of solids fluctuating energy can be expressed as [20]:

$$
\frac{3}{2}\left[\frac{\partial}{\partial t}(\alpha_s\rho_s\Theta_s) + \nabla \cdot (\alpha_s\rho_s\mathbf{u}_s\Theta_s)\right] = \underbrace{(-P_s\mathbf{I} + \tau_s) : \nabla\mathbf{u}_s}_{\text{Production due to shear stress}} + \underbrace{\nabla \cdot (\kappa_\Theta\nabla\Theta)}_{\text{Diffusion}} \tag{5}
$$

$$
- \underbrace{\gamma_{\Theta S}}_{\substack{\text{Dissipation due to inelastic collisions}}} + \underbrace{\Phi_{LS}}_{\substack{\text{Dissipation/Production due to the interaction with the carrier}}}
$$

Rather than solving the complete granular energy balance given in Equation 1, [13] assume the granular energy is in a steady state and dissipated locally and neglect convection and diffusion. Retaining only the generation and the dissipation terms, Equation 1 simplifies to an algebraic expression for the granular temperature:

$$
\left(-p_s\overrightarrow{\mathbf{I}} + \vec{\tau}_s\right) : \vec{\nabla}\vec{u}_s - \gamma_{\Theta s} + \Phi_{LS} = 0 \tag{6}
$$

15

Expression for all the terms can be derived ([40]):

$$\gamma_{\Theta_S} = \frac{12\left(1 - e^2\right)g_0}{d_S\sqrt{\pi}}\rho_S\alpha_S^2\Theta_S^{3/2} \tag{7}$$

$$\phi_{LS} = -3K_{SL}\Theta_S \tag{8}$$

$$p_S = \alpha_S\rho_S\Theta_S + 2\rho_S\left(1 + e\right)\alpha_S^2 g_0\Theta_S) \tag{9}$$

where e is the coefficient of restitution for particle collisions that quantifies the elasticity of particle collisions. (g_0) is the radial distribution function that can also be seen as a probability for interaction between particles. Different models exists, they are formulated is in table 2. The solid bulk viscosity λ_S accounts for the granular particles resistance of compression and expansion. It can be calculated by the following form (Ekambara et al. [13]):

$$\lambda_S = \frac{4}{3}\alpha_S\rho_S d_S g_0\left(1 + e\right)\left(\frac{\Theta_S}{\pi}\right)^{\frac{1}{2}} \tag{10}$$

Then, the solid shear viscosity μ_S based on granular kinetic theory consists of a collisional contribution and from a kinetic contribution. It can be represented as (Gidaspow [40]):

$$\mu_S = \mu_{S,col} + \mu_{S,kin} \tag{11}$$

Table 2 show different Kinetic Theory Correlations for μ_S and g_0.

Remarks:

For granular viscosity:

- Hrenya and Sinclair [43] follow Lun et al. [41] but constrain the mean free path of the particle by a dimension characteristic of the actual physical system. This is opposed to the Lun et al. [41] theory which allows the mean free path to tend toward infinity.

- Lun et al. [41] theory which allows the mean free path to tend toward infinity and the solids viscosities tends toward a finite value as the solids volume fraction tends to zero.

- By constraining the mean free path, the limit of the Hrenya and Sinclair [43] shear viscosity expression correctly tends to zero as the solids volume fraction approaches zero.

16

Table 3: Kinetic Theory Correlations

	Granular viscosity μ_s
Lun et al. [41]	$\frac{4}{5}\alpha_s^2\rho_s d_s g_0(1+e)\sqrt{\frac{\Theta}{\pi}} + \frac{1}{15}\sqrt{\Theta\pi}\frac{\rho_s d_s g_0(1+e)\left(\frac{3}{2}e-\frac{1}{2}\right)\alpha_s^2}{\frac{3}{2}-\frac{1}{2}e} + \frac{1}{6}\sqrt{\Theta\pi}\frac{\rho_s d_s\alpha_s\left(\frac{5}{2}e+\frac{1}{4}\right)}{\frac{3}{2}-\frac{e}{2}} +$ $\frac{10}{96}\sqrt{\Theta\pi}\frac{\rho_s d_s}{(1+e)\left(\frac{3}{2}-\frac{1}{2}e\right)g_0}$
Syamlal et al. [42]	$\frac{4}{5}\alpha_s^2\rho_s d_s g_0(1+e)\sqrt{\frac{\Theta}{\pi}} + \frac{1}{15}\sqrt{\Theta\pi}\rho_s d_s g_0\frac{(1+e)\left(\frac{3}{2}e-\frac{1}{2}\right)}{\frac{3}{2}-\frac{e}{2}}\alpha_s^2 + \frac{1}{12}\frac{\alpha_s d_s\rho_s}{\frac{3}{2}-\frac{e}{2}}\sqrt{\pi\Theta}$
Gidaspow [40]	$\frac{4}{5}\alpha_s^2\rho_s d_s g_0(1+e)\sqrt{\frac{\Theta}{\pi}} + \frac{1}{15}\sqrt{\Theta\pi}\rho_s d_s g_0(1+e)\alpha_s^2 + \frac{1}{6}\sqrt{\Theta\pi}\rho_s d_s\alpha_s + \frac{10}{96}\sqrt{\Theta\pi}\frac{\rho_s d_s}{(1+e)g_0}$
Hrenya and Sinclair [43]	$\frac{4}{5}\epsilon_s^2\rho_s d_s g_0(1+e)\sqrt{\frac{\Theta}{\pi}} + \frac{1}{15}\sqrt{\Theta\pi}\frac{\rho_s d_s g_0(1+e)\left(\frac{3}{2}e-\frac{1}{2}\right)\epsilon_s^2}{\left(\frac{3}{2}-\frac{c}{2}\right)} +$ $\frac{1}{6}\sqrt{\Theta\pi}\frac{\rho_s d_s\epsilon_s\left(\frac{1}{2}\left(1+\frac{\lambda_m f_p}{R}\right)+\frac{3}{4}e-\frac{1}{4}\right)}{\left(\frac{3}{2}-\frac{1}{2}e\right)\left(1+\frac{\lambda_m(p)}{R}\right)} + \frac{10}{96}\sqrt{\Theta\pi}\frac{\rho_s d_s}{(1+e)\left(\frac{3}{2}-\frac{1}{2}e\right)g_0\left(1+\frac{\lambda_m f_p}{R}\right)}$
	Radial Function g_0
Carnahan and Starling [44]	$\frac{1}{1-\epsilon_s} + \frac{3\epsilon_s}{2\left(1-\epsilon_s\right)^2} + \frac{\epsilon_s^2}{2\left(1-\epsilon_s\right)^3}$
Lun and Savage [45]	$\left(1-\frac{\alpha_s}{\alpha_{s,\max}}\right)^{-2.65\alpha_{s,\max}}$
Sinclair and Jackson [46]	$\left[1-\left(\frac{\alpha_s}{\alpha_{s,\max}}\right)^{\frac{1}{3}}\right]^{-1}$
Gidaspow [40]	$\frac{3}{5}\left[1-\left(\frac{\alpha_s}{\alpha_{s,\max}}\right)^{\frac{1}{3}}\right]^{-1}$

- Syamlal et al. [42] solids shear viscosity also tends to zero as the solids volume fraction tends to zero. In this case, however, the solids shear viscosity limit is reached because the kinetic contribution to the solids viscosity is neglected.

For radial function:

- The Carnahan and Starling [44] expression, however, does not tend toward the correct limit at closest solids packing. Because particles are in constant contact at the maximum solid

17

volume fraction, the radial distribution function at contact tends to infinity.

• Alternate expressions to the Carnahan and Starling [44] expression have been proposed by

Gidaspow [40], Lun and Savage [45] and Sinclair and Jackson [46] which tend to the correct

limit at closest packing.

The KTGF models are choosed based on a sensitivity analysis where the Syamlal et al. [42]

model for the granular viscosity gave better results and were more stable, along with Sinclair and

Jackson [46] model for the radial function.

When the solid phase fraction is high in a particular zone of the domain, lots of contacts among

particles occur and a frictional stress derives from them that must be accounted for in the mathe-

matical model. In this state the collisions among particles could not be considered instantaneous

as previously done in the kinetic theory and the frictional stress is accounted for adding a term in

the granular pressure and in the granular viscosity. Hence, the solid shear viscosity μ_S is expressed

by Eq.(12):

$$\mathcal{P}_{\mathfrak{s}} = \mathcal{P}_{\text{kinetic}} + \mathcal{P}_{\text{s,fr}}$$

$$\boldsymbol{\mu}_{\mathfrak{s}} = \mu_{\text{kinetic}} + \mu_{\text{s,fr}}$$

(12)

$$\mathcal{P}_{\mathfrak{s},\mathfrak{fr}} = \mathcal{F}\mathfrak{r}\frac{(\alpha_{\text{s}} - \min{(\alpha_{\text{s}})})^{\mathfrak{n}}}{(\alpha_{\text{s,max}} - \alpha_{\text{s}})^{\mathfrak{p}}}$$

(13)

where $\mathcal{F}\mathfrak{r} = 0.05$, $\mathfrak{n} = 2$ and $\mathfrak{p} = 5$ are empirical constants. The frictional shear viscosity is than expressed by:

$$\boldsymbol{\mu}_{\mathfrak{s},\mathfrak{fr}} = \mathcal{P}_{\text{s,fr}} \sin \delta$$

(14)

being δ the angle of internal friction of the particle.

NB: The frictional stress is added to the stress predicted by the kinetic theory when the solids

volume fraction exceeds a critical value. This value is normally set to 0.5 when the flow is three-

dimensional and the maximum packing limit is about 0.63.

3.2. Pressure drop calculations for single phase flow

The single-phase flow simulations are carried out to validate the modeling approach, the choice

of the turbulence model as well as various essential parameters in order to carry out the treatment

of the area near the wall. Also to validate the surrogates models approach. The pressure drop

data for different water flow rates is recorded for cases of : horizontal pipe, inclined pipe and pipe

with elbow. The results of the CFD code are compared with predicted values from theoretical

correlations found in the literature. Table 4 shows different correlations to calculate the pressure

drop for each setup.

Table 4: Pressure drop correlations

Correlations	Pipe Set up
$\Delta\mathcal{P}_{\mathfrak{f}} = -\mathfrak{f}\dfrac{\rho_{\mathfrak{W}}\mathrm{L}}{\mathrm{D}}\dfrac{\mathrm{U}_{\mathfrak{W}}{}^{2}}{2}$	Horizontal Pipe
$\Delta\mathcal{P} = -\Delta\mathcal{P}_{\mathfrak{f}} - \rho_{\mathfrak{W}}\mathfrak{g}\mathfrak{L}\mathfrak{sin}(\theta)$	Inclined Pipe
$\Delta\mathcal{P} = -\Delta\mathcal{P}_{\mathfrak{f}} - \rho_{\mathfrak{W}}\mathfrak{g}\mathfrak{L}_{\mathrm{inclined}}\mathfrak{sin}(\theta) - \mathcal{K}_{\mathfrak{L}}\dfrac{\rho\mathcal{U}_{\mathfrak{W}}^{2}}{2}$	Pipe with Bend

The implicit relation proposed by Colebrook, Eq.(15), is used to calculate the friction factor
for turbulent flows in rough pipes.

$$\frac{1}{\sqrt{f}} = -2\log\left(\frac{e}{3.71D} + \frac{2.51}{\mathrm{Re}\,\sqrt{f}}\right) \tag{15}$$

where $\frac{e}{D}$ is the relative roughness, and is related the pipe material properties.

3.3. Turbulence model

The turbulence aspect must be ensured when transporting slurry. Since, this will guarantee

the pseudo-homogeneity of the mixture and will subsequently prevent total sedimentation of the

solid phase. In this work, the flow is characterized by a Reynolds number of order of 10^{6}. This

is why the turbulence of water for both single or two phase flow is treated with the standard k-ϵ

model, which is a high Reynolds turbulence model. However, wall functions are used to treat the

boundary-layer development up to the wall. Eq.(16) and Eq.(17) present the model variables, the

turbulent kinetic energy k and the turbulence dissipation rate ϵ respectively:

$$\frac{\partial(\rho_W k_W)}{\partial t} + \frac{\partial\left(\rho_W k_W U_{W_i}\right)}{\partial x_i} = \frac{\partial}{\partial x_j}\left[\left(\mu_W + \frac{\mu_t}{\sigma_k}\right)\frac{\partial k_W}{\partial x_j}\right] + G_k + G_b - \rho_W \varepsilon_W + S_k \tag{16}$$

$$\frac{\partial(\rho_W \varepsilon_W)}{\partial t} + \frac{\partial(\rho_W \varepsilon_W U_{W_i})}{\partial x_i} = \frac{\partial}{\partial x_j}\left[\left(\mu + \frac{\mu_t}{\sigma_\varepsilon}\right)\frac{\partial \varepsilon_W}{\partial x_j}\right] + \frac{C_{1\varepsilon}\varepsilon_W}{k_W}(G_k + C_{3\varepsilon}G_b) - C_{2\varepsilon}\rho\frac{\varepsilon_W^2}{k_W} + S_\varepsilon \quad (17)$$

3.4. Near-wall treatment

The near-wall treatment is done using the wall functions method. The wall functions consist of wall boundary conditions that impose values for the kinetic energy k_P and the dissipation rate ϵ_P variables in the center of the cells near the wall as shown by Eq.(18) and Eq.(19), which bridges turbulent quantities on the wall.

$$k_P = \frac{\sqrt{fU_W^2}}{\sqrt{2C\mu}} \tag{18}$$

$$\epsilon_P = \frac{C_\mu^{3/4} K_P^{3/2}}{k\, y_P} \tag{19}$$

$C_\mu = 0.09$ is a model coefficient of the $k - \epsilon$; $k = 0.41$ is Von Karman constant; y_P is the height to the center of the cell adjacent to the wall and it can be calculated from y^+ according to the Eq.(20).

$$y_p = \frac{y^+ \mu_W}{\rho_W \sqrt{fu_W}} \tag{20}$$

For the inlet turbulence conditions, Eq.(21) present the turbulent kinetic energy (k_{in}) that is obtained from the turbulence intensity (I) and the water inlet velocity (U_W) (Messa and Matoušek [30]):

$$k_{in} = \frac{3}{2}U_W^2 I^2 \tag{21}$$

Next, the length scale (l) of the turbulence at the inlet should be specified. For an internal pipe flow, this is usually $\sim 7\%$ of the pipe diameter. So the turbulent dissipation rate (ϵ_{in}) is calculated as shown in Eq.(22):

$$\epsilon_{in} = C_\mu \frac{k_{in}^{3/2}}{l} \tag{22}$$

4. Methodology

After choosing the mathematical models necessary to simulate the diphasic flow, comes the part of the implementation under the CFD tool. In this work the open-source CFD toolbox open-foam was choosed to perform the simulations, considering its advantages by comparing it with other CFD tools. Figure 3 shows OpenFOAM software advantages.

		OpenFOAM	Commercial Software (ANSYS, STAR-CCM+ etc)
1.	Cost effectiveness	✓	✗
2.	Parallel computing	✓	✓
3.	Source code	✓	✗
4.	Redistribution of code	✓	✗
5.	Collaborative development	✓	✗
6.	Documentation	✗	✓
7.	GUI / user friendliness	✗	✓

Figure 3: Why OpenFOAM ?

The simulation workflow begins with the pre-processing where the geometry along with the mesh are generated, after comes the part of choosing the solver which represent well our model, and then the post-processing where the results of the simulation are visualized. The twoPhaseEuler-Foam solver is the one which represents well our model and since openfoam is an open-source software the solver has been modified to become an isothermal flows solver, since there is no heat exchange between the phases. Then, in the constant file the different forces which act on the flow have been defined according to the assumptions made, where thus the interphase momentum exchange models have been defined. Then the components of the KTGF are implemented taking into consideration the restitution coefficients. The implementation of the model also requires special

attention to the boundary conditions which need a good understanding of the physical phenomenon to define them.

5. Results and discussions

5.1. Single phase flow

To carry out validation of the mathematical model along with the turbulence model and the treatment process for the area near the wall, simulations for a single phase flow are performed for three pipe setups. Moreover, these simulations will help to validate the approach of constructing surrogates models. The predicted values of the theoretical correlations presented in section 3.2, are used to judge the CFD results. The implementation of the models is done under the OpenFOAM software V7. Table 5 summarizes different boundary conditions for different inputs.

Table 5: Summary of the selected boundary conditions

Field	Inlet	Outlet	Solid walls
ϵ_W	fixedValue	zeroGradient	wall function
k_W	fixedValue	zeroGradient	wall function
v_t	zeroGradient	zeroGradient	wallFunction
p	zeroGradient	atmospheric pressure	zeroGradient
U_W	fixedValue	zeroGradient	noSlip

5.1.1. Horizontal pipe

The geometry consists of a $40\,m$ horizontal pipe, with an internal diameter of $0.9\,m$. Figure 4(a) and 4(b), shows a 2D section and the 3D meshed geometry. GMSH software was used to generate a specific mesh which takes into account the near-wall refinement by calculating the height of the first cell on the wall, with a precise magnification ratio which is linked to y^+ while approaching the center of the pipe. The flow consists of water with a density $\rho = 1000 kg/m^3$. The Wall roughness is set at $0.045\,mm$. The inlet velocity is in ranges of 1 to 3 m/s. The pressure at the outlet is fixed

22

as atmospheric pressure. The latter initial condition is the same for the next simulations of inclined and bended pipe in subsections 3.1.2 and 3.1.3 respectively.
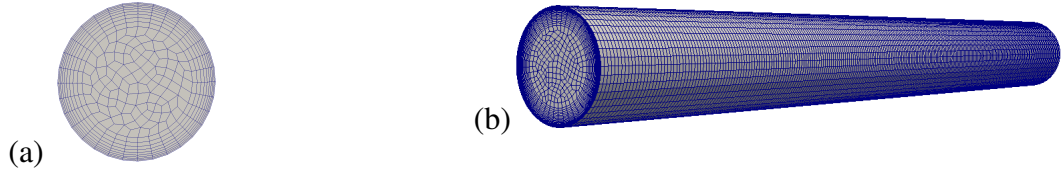
GPU

Figure 4: Horizontal pipe geometry: (a) Cross-section mesh, (b) Profile mesh

For a horizontal pipe, we have regular pressure drops, which are generated by the friction of the fluid on the internal wall of the pipe throughout its passage. They depend on, the length of the pipe, the relative roughness of the pipe, the speed of the fluid circulating in the pipe (U_{in} m/s), as presented in table 1. Therefore, As can be seen in Figure 5, the pressure losses are increasing relatively with inlet velocities. For this current case of a horizontal pipe, experimental data were found for water flow in (Gillies et al. [47]), and also a good agreement was found with cfd results as shown in Figure 5.

The mean average percentage error is defined as follows:

$$\text{MAPE} = \left\{ \frac{1}{n} \sum_{k=1}^{n} \left[\left| \frac{(dp/dx)_{\text{pred}} - (dp/dx)_{\text{theory}}}{(dp/dx)_{\text{theory}}} \right| \right] \right\} 100$$
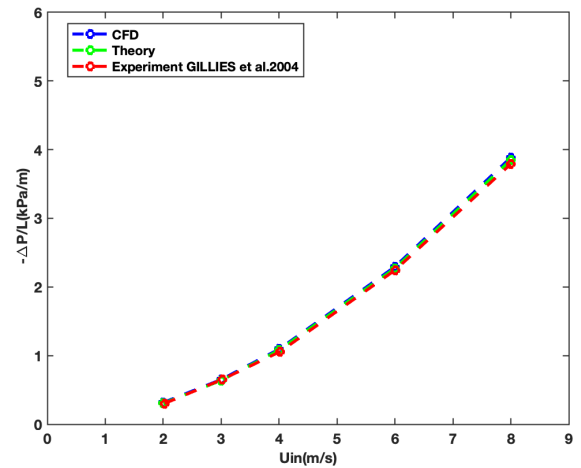
MAPE = 1.21 %

Figure 5: Pressure drop in horizontal pipe. Present pressure drops from CFD simulations versus empirical formula in table 4 and experimental measurements.

23

5.1.2. Inclined pipe

In this section, the geometry consists of a 40 *m* inclined pipe with 0.9 *m* diameter and a 5.73

degree negative slope. Figure 6(a) and 6(b) show the cross-section and profile mesh.
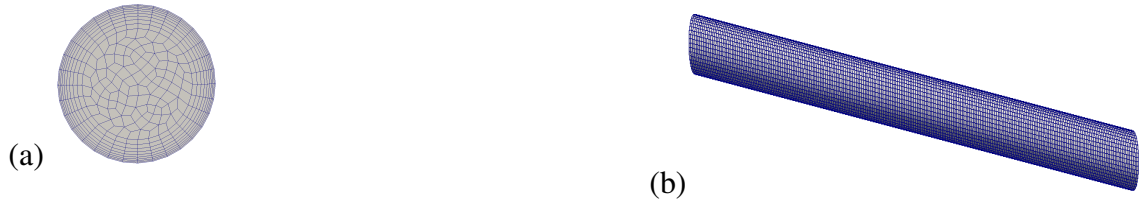
(a)

(b)

Figure 6: Inclined pipe geometry: (a) Cross-section mesh, (b) Profile mesh

Concerning this pipe setup, it is characterized by a changing elevation. Consequently, at the

end of the inclined pipe there is the full weight of fluid pushing down on that point and due to

this, the pressure at that point increases. Therefore, there is a pressure gain in the pipe as the fluid

goes down. The total pressure difference can be calculated by adding the hydrostatic pressure to

the friction component as in table 4. Figure 7, show the pressure gradient as a function of inlet

velocities. As noticed the pressure gain decreases while increasing the velocity, and this comes

back to the augmentation of friction losses.

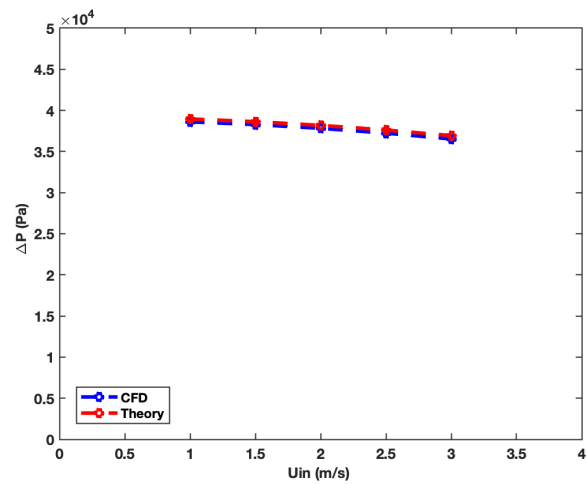The mean average percentage error (MAPE) = 0.97 %

Figure 7: Pressure drop in inclined pipe

24

5.1.3. Bended pipe

For this setup, the geometry consists of a 45 degree bended pipe, of 6 m equivalent length with 0.9 m diameter. Figure 8(a) and 8(b) show the cross-section and profile mesh.
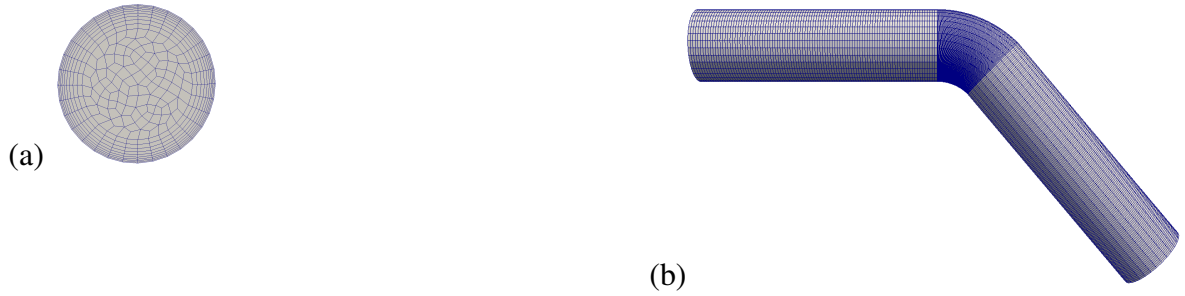

(a)

(b)

Figure 8: Bended pipe geometry: (a) Cross-section mesh, (b) Profile mesh

This pipe setup is more complex, since in addition to the previously discussed components of the kinetic losses, another component is added namely the singular pressure drop as in table 4. The singular pressure drops are mainly due to the geometric modification of the pipe, such as changes of direction like bends. Figure 9 shows that the pressure loss is increased in such geometries.
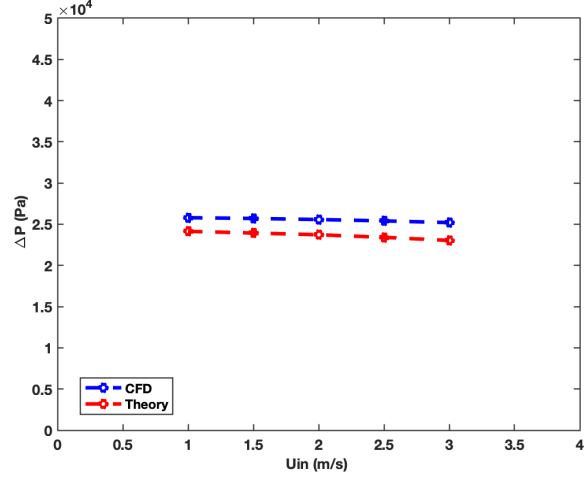
25

The mean average percentage error (MAPE) = 7.99 %

Figure 9: Pressure drop in bended pipe. The empirical formula slightly underestimates the pressure drop versus the CFD simulations

The pressure drop formulae constitute surrogate models for pressures calculations in piping systems with newtonian fluids such as water. From the previous analysis we see that CFD reproduces very well the pressure drop measurement and the empirical models fits the CFD results for the classical geometrical configurations. Hence, one can consider for example computing other pressure drop models for Newtonien fluids but for much more complex geometries, where experiments may be complex or time consuming to conduct. In the next section we will consider a different case, where the complexity is introduced in the fluid itself. And the aim is to use the CFD approach to develop pressure drop models for complex fluids.

5.2. Two phase flow

An attempt to simulate the behaviour of a sediment-water mixture during its transportation through a pipe has been made, using the twoPhaseEulerFoam solver available in the 6.0 release of the open-source CFD toolbox OpenFOAM. The geometry used consisted of a pipe of length L = 0.02 m, a diameter D = 0.0001 m. The flow is laminar with Re = 144, , $\rho_S = 1,450 kg/m^3$, $\rho_W = 1,027 kg/m^3$, $V_{mixture} = 1 m/s$, $d_S = 70 \mu m$, $\mu_W = 0.00891 kg/m.s$, $\alpha_{0S} = 30\%$, $P_0 = 10^5 Pa$. Figure 6 and 7, show the 2D and 3D meshed geometry. OpenFOAM's meshing utility blockMesh

was used to generate structured orthogonal meshes about 200 cells along the pipe.

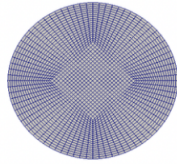- **Pre-processing: 2D and 3D meshed geometry**
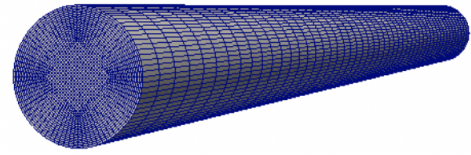

Figure 10: Cross-section mesh

Figure 11: 3D pipe mesh

- **Post-processing**

Figure 8 and 9 show the solid concentration for the cross-section of the pipe and along the pipe respectively. These first results show an agreement with one of the types of two-phase flows found in the literature, which is a sliding bed flow. While, figure 10 shows that the condition of the fractional volumes sum for the two phases is equal to 1, throughout the diameter in the pipe outlet.
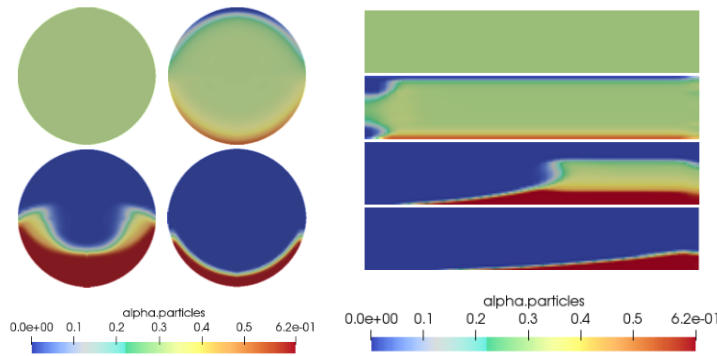

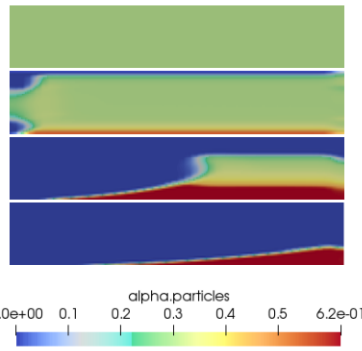Figure 12: Cross-section Concentration at the outlet
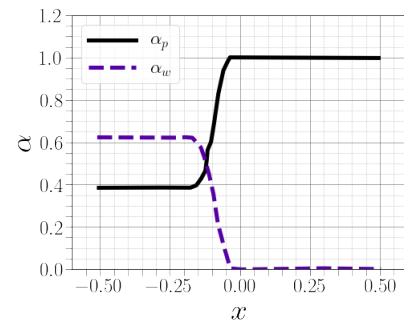
Figure 13: Concentration along the pipe

Figure 14: Volume fraction of both phases

Two phase simulations were presented by authors in (Elkarii et al. [33]), where a slurry of mono-dispersed spherical polystyrene beads with rhodorsil silicone oil were simulated in a laminar flow.

Figure 15 shows the evolution of the solid concentration profile of the mixture over time.
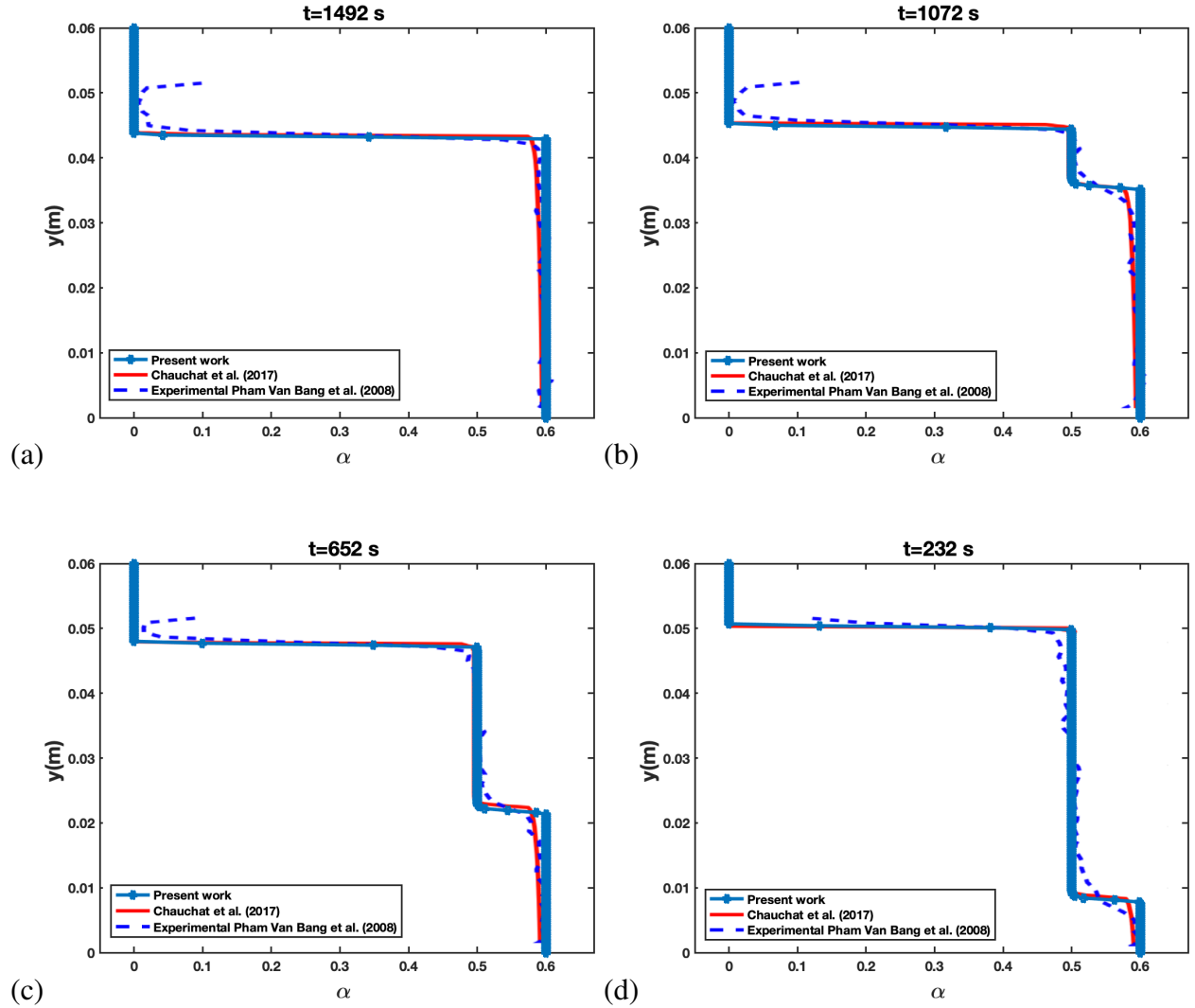
Figure 15: Sediment concentration profiles over time (a) At t = 232 s, (b) t = 652 s (c) t = 1072 s (d) t = 1492 s

The previous study (Elkarii et al. [33]), validates the model for its capability to reproduce and predict high volume concentration profiles up to 60 %. The validation case consists of a sedimentation of non-cohesive particles by Chauchat et al. [48], based on experimental data from (Pham Van Bang et al. [49]). The sedimentary phase was also modeled as continuous and consecutive laws were adopted to take sedimentary constraints into account.

However, to approach the simulation of a real slurry flow, the turbulence aspect must be added to prevent sedimentation problems. Therefore, in this part, CFD simulations were performed to fit the experimental results of a turbulent flow of water-sand slurry under isothermal conditions, reported by Gillies et al. [47]. Experimental data consists of pressure drops along the pipe, particle concentration profiles and particles velocity profiles at the pipe outlet. The simulation domain consists of a 10 m long pipe. boundary conditions set are the inlet, the outlet and the lateral surface which is referenced as walls, are presented in the table 6. The mass flow rates of the two phases, $\dot{m}_W$ and $\dot{m}_S$ are fixed at the inlet boundary, and calculated as in Eq.(23), the turbulent kinetic energy of the liquid, k_{in}, and its dissipation rate, ϵ_{in}, were also fixed as in Eq.(21) and Eq.(22).

$$\dot{m}_W = \alpha_W \rho_W U_W A; \quad \dot{m}_S = \alpha_S \rho_S U_S A \tag{23}$$

Table 6: Summary of the selected boundary conditions

Field	Inlet	Outlet	Solid walls
α_s	fixedValue	zeroGradient	zeroGradient
α_W	fixedValue	zeroGradient	zeroGradient
ϵ_W	fixedValue	zeroGradient	wall function
k_W	fixedValue	zeroGradient	wall function
v_t	zeroGradient	zeroGradient	wall function
p	fixedFluxPressure	atmospheric pressure	zeroGradient
θ_p	fixedValue	zeroGradient	JohnsonJacksonParticleTheta
U_W	mass flow rate	zeroGradient	noSlip
U_S	mass flow rate	zeroGradient	JohnsonJacksonParticleSlip

The numerical simulations performed in this section, uses the same mesh configuration, as in section 5.1, except that the meshes have been refined in all directions. The flow is characterized by high inlet velocities ranging up to 8 m/s. Two diameters of particles are considered, along with different solid concentrations. The physical parameters used are sand density $\rho_s = 2650\ kg/m^3$, water density $\rho_W = 1000\ kg/m^3$, and water viscosity $\mu_w = 10^{-3} kg/m.s$. The radial distributions of

sand particles for two inlet concentrations are presented in figure 16. Regarding the experimental results, the solid concentration profile varies slightly along the diameter of the pipe ($0.19 < \alpha_s < 0.24$). The present simulation in figure 16(a) agrees fairly well with the experiments in the bulk flow ($0.2 < r/D < 0.9$), whereas the model underestimate the experimental values of α_s near the upper wall ($r/D > 0.9$), and on the other hand, overestimate them along the lower wall ($r/D < 0.2$). In the present model, it can be attributed to the none total control of the turbulent viscosity term, which promotes the phenomenon of sedimentation, resulting in a non-homogeneous concentration profile. On figure 16(b) the solid concentration is increased up to 33 %, but, the same behavior is always observed, and corresponds to a pseudo-homogeneous flow with formation of a small bed of particles.
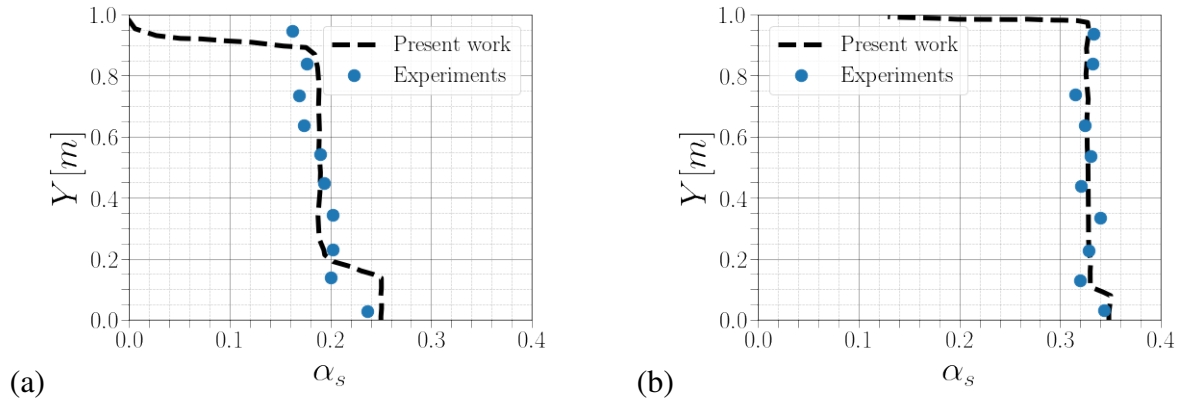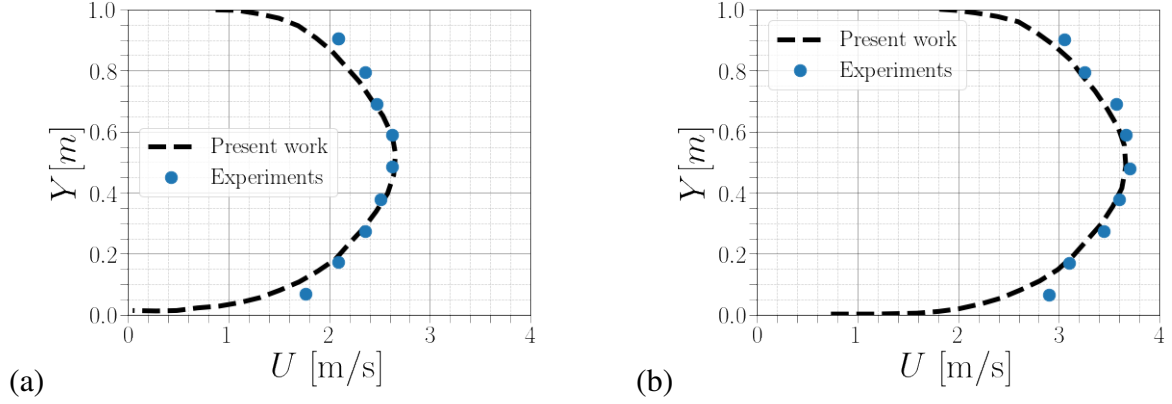

Figure 16: Radial distributions of the volume fraction of sand particles of $d_p = 0.09mm$ for $U_{in} = 3m/s$: (a) ($\alpha_{s,in} = 0.19$), (b) ($\alpha_{s,in} = 0.33$)

The particles velocity profiles for $U_{in} = 2m/s$ and $U_{in} = 3m/s$ are presented in figure 17(a) and 17(b) respectively. On the contrary to the concentration distribution, the present model predicts the right profile of velocity. It is remarked that the axial average velocities distributions are symmetrical, and they agree almost exactly to a classic turbulent parabolic profile. This comes down to the fact that the presence of particles does not greatly influence the current field. This is explained by the constant solid concentration around the value 0.2 for the entire pipe and the dynamic viscosity of the fluid then varies slightly.

30

463

(a)   (b)

464

Figure 17: Radial distributions of the mean axial velocity of sand particles at the outlet of the pipe, for $\alpha_s in = 0.19$ and $d_p = 0.09mm$: (a) ($Uin = 2m/s$), (b) ($Uin = 3m/s$).

Figure 18 (a) and (b) shows the variations of the pressure drop per unit length $\Delta P/L$ with the inlet velocity of the mixture U_{in}. The present simulations obtained for two different particles diameters $d = 0.09mm$ and $d = 0.27mm$, for nearly the same inlet concentration, and for a high velocities. Experimental data from (Gillies et al. [47]) is used as a validation for current simulations. The pressure drop analyzed in current simulations augments almost linearly with U_{in}. As anticipated, the pressure drop increases because of the increased values of friction losses. Results fit well in figure 18 (a) for $d = 0.09mm$, However, discrepancies are higher at high velocities. Contrary to figure 18 (b) for $d = 0.27mm$, a very good agreement is observed at high velocities, and a large gap is visible at low input velocities $U_{in} \leq 3m/s$.

31

474
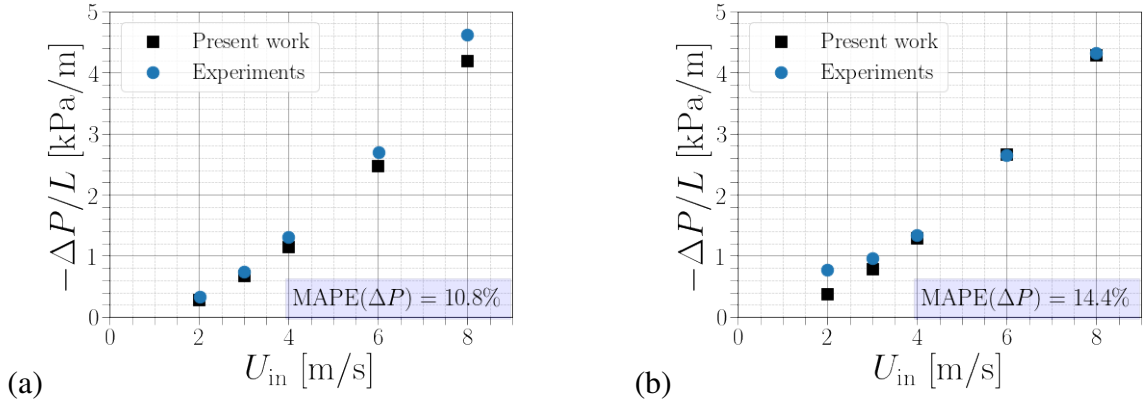
Figure 18: Pressure drop per unit of length $\Delta P/L$ versus slurry velocity: (a) ($\alpha_S = 0.19$, $d = 0.09mm$), (b) ($\alpha_S = 0.20$, $d = 0.27mm$).

It is also noted, that coarser particles compared to smaller ones, have superior pressure drop at lower flow rates and have an inferior one at higher flow rates. The reason behind this, is that the coarser particles at lower speeds deposit more which comes down to the gravitational effect, and subsequently, the amount of particles in the bed increases which leads to more frictions. While, in the case of smaller particles at higher velocities, the pressure losses are bigger due to the larger surface area of the material.

5.3. Surrogate model

Once the CFD results are validated with experimental data, this work aims to construct a surrogate model for the pressure drops for a two-phase flow within a piping system. The proposed model uses the empirical formula in Table 4 for the pressure losses due to frictions for horizontal pipes. The density, however, is that of the water-sand mixture. The model has been calibrated to find the optimal friction factor f, that fit well with the CFD results trough a minimization process (figure 19), for different solid concentration α_s and two particle sizes d_p.
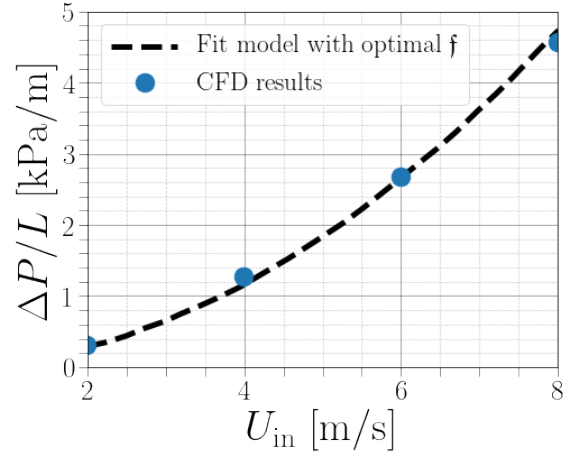
Figure 19: Example of fitting of the empirical formula of pressure drop with the CFD results for $\alpha_S = 0.19$ and $d_p = 0.09mm$.

Figure 20 shows the variation of the calibrated friction factor $f(\alpha_s, d_p)$ as function of the solid volume concentration for two different particle sizes.

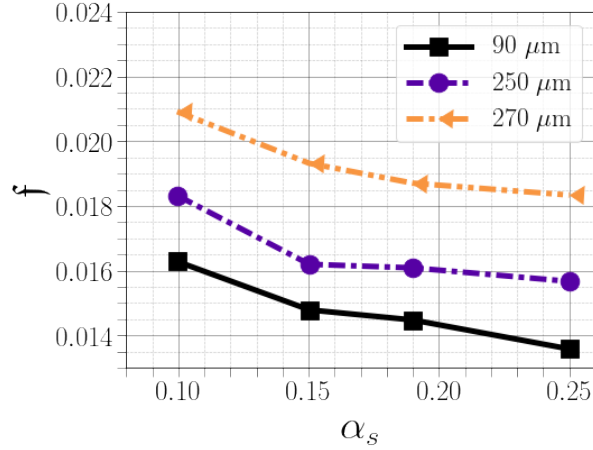Figure 20: Optimal calibrated values of the friction factor along with the variation of the solid concentration for particles with diameter $d_p = 0.09$ and $d_p = 0.27$.

According to figure 20, one can for example for a given α_S and the specified particle diameters, interpolate to find values of f and then predict the pressure drop by substituting the found value of f in the empirical formula.

33

5.3.1. Generalized Polynomial Chaos (GPC)

6. Conclusion

This paper is about modelling slurry flows in pipelines. A quite vast review of the literature of previous CFD investigations on slurry flow in horizontal pipelines was realized first, to decide on the relevant modeling approaches as well as the corresponding mathematical models. Based on this state of art, the two fluid model was the one choosed to work with, because it has the ability to capture well the physics of such complex flows while ensuring moderate computing time. Then, it was decided to begin with simulations of single phase flow into different pipe setups, to validate the turbulence model and to validate the approach of constructing a surrogate model throughout 3D numerical simulations. In this part CFD results matches the empirical data and theoretical models for pressure loss, also a really good agreement versus experimental data even at high velocities was found. After that, two phase flow simulations are performed, to investigate the physical phenomenons within such flows.

CFD results showed high level correspondence with the presented experimental data. Starting with the results of the pressure drops, the overall mean relative errors are limited to 15 %, and this validates our use of the CFD experiments to build a pressure loss surrogate model. However, some deviation is noted for the development of the solid concentration profile along the diameter of the pipe. Roughly speaking, the validity of the mathematical model under the given range conditions is proven, and these results will allow us to construct pressure loss laws. Finally, a surrogate model is tested, which makes it possible to predict the pressure drops as a function of the variation in the solid concentration without performing simulations. Further tests are to come where greater variation in parameters such as solids concentration, particle size and even pipe diameter will be taken into account to increase result's accuracy. This type of surrogate models can be incorporated for plant's operators to predict pressure drops as a function of the variation of different flow parameters.

34

References

[1] S. Lahiri, K. Ghanta, Regime identification of slurry transport in pipelines: A novel modelling approach using ann & differential evolution, Chemical Industry and Chemical Engineering Quarterly 16 (2010) 329–343. doi:10.2298/CICEQ091030034L.

[2] B. Xia, D. Sun, Applications of computational fluid dynamics (cfd) in the food industry: a review, Computers and Electronics in Agriculture 34 (2002). doi:10.1016/s0168-1699(01)00177-6.

[3] J. Wanot, Computational fluid dynamics methods in ship design, R&D projects (1996), Germany (1996). doi:10.1036/1097-8542.YB001340.

[4] C. T. Crowe, J. D. Schwarzkopf, M. Sommerfeld, Y. Tsuji, Multiphase flows with droplets and particles, CRC press, 2011.

[5] J. Capecelatro, O. Desjardins, Eulerian–lagrangian modeling of turbulent liquid–solid slurries in horizontal pipes, International Journal of Multiphase Flow 55 (2013) 64–79. doi:10.1016/j.ijmultiphaseflow.2013.04.006.

[6] H. K. Versteeg, W. Malalasekera, An introduction to computational fluid dynamics: the finite volume method (2007).

[7] S. K. Arolla, O. Desjardins, Transport modeling of sedimenting particles in a turbulent pipe flow using euler–lagrange large eddy simulation, International Journal of Multiphase Flow 75 (2015) 1 – 11. doi:10.1016/j.ijmultiphaseflow.2015.04.010.

[8] A. Uzi, A. Levy, Flow characteristics of coarse particles in horizontal hydraulic conveying, Powder Technology (2017). doi:10.1016/j.powtec.2017.11.067.

[9] J. Ling, P. Skudarnov, C. Lin, M. Ebadian, Numerical investigations of liquid–solid slurry flows in a fully developed turbulent flow region, International Journal of Heat and Fluid Flow 24 (2003) 389–398. doi:10.1016/s0142-727x(03)00018-3.

[10] C. Lin, M. Ebadian, A numerical study of developing slurry flow in the entrance region of a horizontal pipe, Computers & Fluids 37 (2008) 965–974. doi:10.1016/j.compfluid.2007.10.008.

[11] R. Silva, P. Faia, F. Garcia, M. Rasteiro, Characterization of solid–liquid settling suspensions using electrical impedance tomography: A comparison between numerical, experimental and visual information, Chemical Engineering Research and Design 111 (2016) 223–242. doi:10.1016/j.cherd.2016.05.013.

[12] F. H. Hernandez, A. J. Blanco, L. Rojas-Solorzano, Cfd modeling of slurry flows in horizontal pipes 48401 (2008) 857–863.

[13] K. Ekambara, R. S. Sanders, K. Nandakumar, J. H. Masliyah, Hydrodynamic simulation of horizontal slurry pipeline flow using ansys-cfx, Industrial & Engineering Chemistry Research 48 (2009) 8159–8171. doi:10.1021/ie801505z.

[14] L. Chen, Y. Duan, W. Pu, C. Zhao, Cfd simulation of coal-water slurry flowing in horizontal pipelines, Korean Journal of Chemical Engineering 26 (2009) 1144–1154. doi:10.1007/s11814-009-0190-y.

[15] B. M. Bossio, A. J. Blanco, F. H. Hernandez, Eulerian-eulerian modeling of non-newtonian slurries flow in horizontal pipes 43727 (2009) 525–533. doi:10.1115/FEDSM2009-78019.

[16] C. L. Antaya, K. F. K. Adane, R. S. Sanders, Modelling concentrated slurry pipeline flows 44755 (2012) 1659–1671. doi:10.1115/FEDSM2012-72379.

[17] D. Kaushal, T. Thinglas, Y. Tomita, S. K. H. Tsukamoto, Cfd modeling for pipeline flow of fine particles at high concentration, International Journal of Multiphase Flow 43 (2012) 85–100. doi:10.1016/j.ijmultiphaseflow.2012.03.005.

[18] Y. Jiang, P. Zhang, Numerical investigation of slush nitrogen flow in a horizontal pipe, Chemical Engineering Science 73 (2012) 169–180. doi:10.1016/j.ces.2012.01.027.

[19] Y. Jiang, P. Zhang, Pressure drop and flow pattern of slush nitrogen in a horizontal pipe, AIChE Journal 59 (2013) 1762–1773. doi:10.1002/aic.13927.

[20] J. Wang, S. Wang, T. Zhang, Y. Liang, Numerical investigation of ice slurry isothermal flow in various pipes, International Journal of Refrigeration 36 (2013). doi:10.1016/j.ijrefrig.2012.08.007.

[21] G. V. Messa, M. Malin, S. Malavasi, [asme asme 2013 pressure vessels and piping conference - paris, france (sunday 14 july 2013)] volume 4: Fluid-structure interaction - numerical prediction of pressure gradient of slurry flows in horizontal pipes, 2013. doi:10.1115/pvp2013-97460.

[22] G. V. Messa, M. Malin, S. Malavasi, Numerical prediction of fully-suspended slurry flow in horizontal pipes, Powder Technology 256 (2014) 61–70. doi:10.1016/j.powtec.2014.02.005.

[23] G. V. Messa, S. Malavasi, Improvements in the numerical prediction of fully-suspended slurry flow in horizontal pipes, Powder Technology 270 (2015) 358–367. doi:10.1016/j.powtec.2014.10.027.

[24] M. K. Gopaliya, D. R. Kaushal, Analysis of effect of grain size on various parameters of slurry flow through pipeline using cfd, Particulate Science And Technology (2015). doi:10.1080/02726351.2014.971988.

[25] S. A. Hashemi, R. B. Spelay, K. F. K. Adane, R. Sean Sanders, Solids velocity fluctuations in concentrated slurries, The Canadian Journal of Chemical Engineering 94 (2016) 1059–1065. doi:10.1002/cjce.22492.

[26] N. Kumar, M. K. Gopaliya, D. Kaushal, Experimental investigations and cfd modeling for flow of highly concentrated iron ore slurry through horizontal pipeline, Particulate Science and Technology 37 (2017) 232–250.

[27] M. K. Singh, S. Kumar, D. Ratha, Computational analysis on disposal of coal slurry at high solid concentrations through slurry pipeline, International Journal of Coal Preparation and Utilization 40 (2017) 116–130.

[28] M.-z. Li, Y.-p. He, Y.-d. Liu, C. Huang, Hydrodynamic simulation of multi-sized high concentration slurry transport in pipelines, Ocean Engineering 163 (2018) 691–705. doi:10.1016/j.oceaneng.2018.06.046.

[29] M. Li, Y. He, Y. Liu, C. Huang, Effect of interaction of particles with different sizes on particle kinetics in multi-sized slurry transport by pipeline, Powder Technology (2018). doi:10.1016/j.powtec.2018.07.088.

[30] G. V. Messa, V. Matoušek, Analysis and discussion of two fluid modelling of pipe flow of fully suspended slurry,

Powder Technology (2020). doi:10.1016/j.powtec.2019.09.017.

[31] A. Rabhi, A. Chkifa, S. Benjelloun, A. Latifi, Surrogate-based modeling in flotation processes, Computer Aided chemical engineering 43 (2018) 229–234.

[32] Y. Seong, C. Park, J. Choi, I. Jang, Surrogate model with a deep neural network toevaluate gas–liquid flow in a horizontal pipe, Energies 13 (2020) 968. doi:doi:10.3390/en1304096.

[33] M. Elkarii, C. Bouallou, A. Ratnani, Towards modelling a diphasic flow using the CFD technique to achieve a digital twin of a Phosphate slurry piping process, Chemical Engineering Transactions 81 (2020) 757–762.

[34] A. Passalacqua, R. O. Fox, Implementation of an iterative solution procedure for multi-fluid gas–particle flow models on unstructured grids, Powder Technology 213 (2011) 174–187.

[35] D. A. Drew, S. L. Passman, Theory of multicomponent fluids, volume 135, Springer Science & Business Media, 2006.

[36] M. R. Maxey, J. J. Riley, Equation of motion for a small rigid sphere in a nonuniform flow, The Physics of Fluids 26 (1983) 883–889.

[37] C. Y. Wen, Y. H. Yu, A generalized method for predicting the minimum fluidization velocity, AIChE Journal 12 (1966) 610–612.

[38] T. R. Auton, J. C. R. Hunt, M. Prud'Homme, The force exerted on a body in inviscid unsteady non-uniform rotational flow, Journal of Fluid Mechanics 197 (1988) 241–257.

[39] J. González, N. Sabirgalieva, L. Rojas-Solorzano, G. Zarruk, Numerical simulation of slurry flows in heterogeneous and saltation regimes in horizontal pipelines, Chemical Engineering Transactions 57 (2017) 1279–1284. doi:10.3303/CET1757214.

[40] D. Gidaspow, Multiphase flow and fluidization: Continuum and kinetic theory descriptions by d. gidaspow, The Canadian Journal of Chemical Engineering 73 (1994) 784–784. doi:10.1002/cjce.5450730523.

[41] C. Lun , S. Savage, D. Jeffrey, N. Chepurniy , Kinetic theories for granular flow: Inelastic particles in couette flow and slightly inelastic particles in a general flowfield, Journal of Fluid Mechanics 140 (1984) 223 – 256. doi:10.1017/S0022112084000586.

[42] M. Syamlal, W. Rogers, T. J. O'Brien, Mfix documentation theory guide (1993). doi:10.2172/10145548.

[43] C. M. Hrenya, J. L. Sinclair, Effects of particle-phase turbulence in gas-solid flows, AIChE Journal 43 (1997) 853–869. doi:10.1002/aic.690430402.

[44] N. F. Carnahan, K. E. Starling, Equation of state for nonattracting rigid spheres, The Journal of Chemical Physics 51 (1969) 635–0. doi:10.1063/1.1672048.

[45] C. Lun, S. Savage, The effects of an impact velocity dependent coefficient of restitution on stresses developed by sheared granular materials, Acta Mechanica 63 (1986) 15–44. doi:10.1007/BF01182538.

[46] J. L. Sinclair, R. Jackson, Gas-particle flow in a vertical pipe with particle-particle interactions, AIChE Journal 35 (1989) 1473–1486. doi:10.1002/aic.690350908.

37

[47] R. G. Gillies, C. A. Shook, J. Xu, Modelling heterogeneous slurry flows at high velocities, The Canadian Journal of Chemical Engineering 82 (2004). doi:10.1002/cjce.5450820523.

[48] J. Chauchat, Z. Cheng, T. Nagel, C. Bonamy, T.-J. Hsu, Sedfoam-2.0: A 3-d two-phase flow numerical model for sediment transport, Geoscientific Model Development 10 (2017) 4367–4392. doi:10.5194/gmd-10-4367-2017.

[49] D. Pham Van Bang, E. Lefrançois, P. Sergent, F. Bertrand, Expérimentation par irm et modélisation par éléments finis de la sédimentation-consolidation des vases, La Houille Blanche (2008) 39–44. doi:10.1051/lhb:2008025.